Multi-spectral intravascular photoacoustic/ultrasound/optical coherence tomography tri-modality system with a fully-integrated 0.9-mm full field-of-view catheter for plaque vulnerability imaging

JI LENG,[1,5] JINKE ZHANG,[1,5] CHENGUANG LI,[2,5] CHENGYOU SHU,[1] BOQUAN WANG,[1] RIQIANG LIN,[1] YANMEI LIANG,[3] [ID] KEQIANG WANG,[2] LI SHEN,[2] KWOK-HO LAM,[4] ZHIHUA XIE,[1,6] XIAOJING GONG,[1,7] JUNBO GE,[2,8] AND LIANG SONG[1,9]

[1]*Research Center for Biomedical Optics and Molecular Imaging, Shenzhen Key Laboratory for Molecular Imaging, Guangdong Provincial Key Laboratory of Biomedical Optical Imaging Technology, CAS Key Laboratory of Health Informatics, Shenzhen Institute of Advanced Technology, Chinese Academy of Sciences, Shenzhen, 518055, China*

[2]*Department of Cardiology, Shanghai Institute of Cardiovascular Diseases, Zhongshan Hospital, Fudan University, Shanghai, China*

[3]*Institute of Modern Optics, Nankai University, Tianjin Key Laboratory of Micro-scale Optical Information Science and Technology, Tianjin, 300350, China*

[4] *Department of Electrical Engineering, Research Institute for Smart Energy, The Hong Kong Polytechnic University, Hung Hom, Kowloon, Hong Kong, China*

[5]*Equal contribution*

[6]*zh.xie@siat.ac.cn*

[7]*xj.gong@siat.ac.cn*

[8]*jbge@zs-hospital.sh.cn*

[9]*liang.song@siat.ac.cn*

Abstract: Myocardial infarctions are most often caused by the so-called vulnerable plaques, usually featured as non-obstructive lesions with a lipid-rich necrotic core, thin-cap fibroatheroma, and large plaque size. The identification and quantification of these characteristics are the keys to evaluate plaque vulnerability. However, single modality intravascular methods, such as intravascular ultrasound, optical coherence tomography and photoacoustic, can hardly achieve all the comprehensive information to satisfy clinical needs. In this paper, for the first time, we developed a novel multi-spectral intravascular tri-modality (MS-IVTM) imaging system, which can perform 360° continuous rotation and pull-backing with a 0.9-mm miniature catheter and achieve simultaneous acquisition of both morphological characteristics and pathological compositions. Intravascular tri-modality imaging demonstrates the ability of our MS-IVTM system to provide macroscopic and microscopic structural information of the vessel wall, with identity and quantification of lipids with multi-wavelength excitation. This study offers clinicians and researchers a novel imaging tool to facilitate the accurate diagnosis of vulnerable atherosclerotic plaques. It also has the potential of clinical translations to help better identify and evaluate high-risk plaques during coronary interventions.

1. Introduction

Despite advances in medical therapy and revascularization, cardiovascular disease (CVD) remains the world's leading cause of death and causes extensive disability [1–3]. Many of these coronary events are attributed to the so-called vulnerable coronary plaques, defined as non-obstructive

lesions that are at elevated risk of rupture [4,5]. The early evaluation of the vulnerability of plaques has a high priority in the prevention of cardiovascular diseases. Several characteristics have been recognized as the key factors of plaque vulnerability, including lipid-rich necrotic core, thin-cap fibroatheroma, and plaque burden [4–6]. Early studies focused on the morphological quantification of plaque burden, stenosis, and fibrous cap, whereas recent researches emphasized that lipid core burden index, which indicates the richness of lipid in plaques, is also highly associated with patient-level major adverse cardiac events [7–9]. Acquiring the plaque morphological information to evaluate the plaque burden and thin-cap fibroatheroma, as well as identifying and quantifying lipid component at the same time, are always what the researchers and physicians expect to evaluate the vulnerability of plaques by using intravascular imaging modalities.

The commonly used clinical intravascular imaging modalities are IVUS and IVOCT. Intravascular ultrasound (IVUS) is helpful to evaluate the plaque burden and the degree of stenosis of artery lumen, and thus has been widely used as a common diagnostic procedure in cardiology currently [10]. Intravascular optical coherence tomography (IVOCT) is indispensable for evaluating the thickness of the fibrous cap covering the lipid core of the atheroma due to its micro-scale spatial resolution [11,12]. Both IVUS and IVOCT are primarily sensitive to the structural information of the artery wall. In addition to morphological imaging, several functional imaging methods have been proposed, including near-infrared fluorescence imaging (NIRF) [13,14], near-infrared spectroscopy (NIRS) [15], and Raman spectroscopy [16]. These methods have the ability to quantify the functional information of plaques, such as the richness of lipid core plaques [7–9]. However, limited penetration depth and lack of depth resolution make these purely optical imaging methods difficult to image or locate interested targets beneath deep tissues. Due to the nature of optical excitation and ultrasonic detection, the emerging intravascular photoacoustic imaging (IVPA) can image beyond the ballistic regime while maintaining optical contrast, which makes photoacoustic imaging capable of locating and imaging lipid core in both lateral and depth directions [17,18]. Importantly, the photoacoustic modality can also provide absorption spectroscopic information of matters. With multi-wavelength excitation, the spectroscopic photoacoustic imaging is capable of distinguishing lipids from other components and quantifying the lipid concentration [19,20], which is significant in evaluating lipid deposits for the diagnosis of vulnerable atherosclerotic plaques.

However, there is no current single modality intravascular imaging method that can completely meet the satisfy of diagnosing vulnerable atherosclerotic plaques. The plaque vulnerability is highly related to the structure of the plaque as well as its chemical composition [21]. The clinicians require multiple features to make comprehensive identification [7,22,23]. Thus, it is important to develop an intravascular imaging technology combining multiple modalities to evaluate the vulnerable plaques. Several dual-modality imaging systems have been proposed for evaluation of total plaque burden, fibrous cap, and providing the lipid distribution information [17,24–26]. However, none of the dual-modality imaging methods can provide the information of fibrous cap, lipid core, and plaque burden simultaneously. Recently, several PA/US/OCT tri-modality systems were developed and applied into biomedical imaging: a 5-mm prototype endoscopic probe, which consisted of an OCT fiber, a photoacoustic-light-delivering fiber, and a US transducer, enabled PA/US/OCT tri-modality imaging of ovarian tissue from a patient with endometriosis [27], but the size of the probe makes it not suitable for imaging human coronary artery (3-4 mm) [28]; a 1-mm miniature endoscope probe, which was physically integrated, was developed to image human artery with lipid-rich plaques by rotatory scanning the sample and mouse ear by horizontal scanning [29,30]. In these previous studies, the problems of oversize and non-rotation limit the translation of the tri-modality system into intravascular clinical applications. In addition, the benefits of photoacoustic in functional imaging have not been fully developed in current tri-modality systems.

Here, we introduce a novel multi-spectral intravascular tri-modality (MS-IVTM) imaging system with three modalities fully integrated: photoacoustic, OCT, and US imaging, through a single miniature catheter (0.9 mm). It can perform three-dimensional intravascular imaging with 360-degree continuous rotation and pull-backing synchronously. Meanwhile, the MS-IVTM system also achieved multi-wavelength photoacoustic imaging of lipid components and evaluated their concentration.

2. Materials and methods

2.1. MS-IVTM system design

The custom-built tri-modality imaging system was fully integrated as shown in Fig. 1(a). In the photoacoustic modality, a pulsed optical parameter oscillator laser (OPO) laser (Vibrant 355 II HE, OPOTek, USA) was used for photoacoustic signal excitation, covering the wavelength range of lipid absorption peaks. The output laser beam from OPO was focused into a multimode fiber (MMF, FG105LCA, Thorlabs, USA), which has a broad operation wavelength range (400 nm - 2400 nm). In the OCT modality, a swept-frequency laser (AXA10823-8, Axsun, Canada) was used as the OCT source. The swept-frequency optical beam was directly coupled into a single-mode fiber (SMF, SMF-28-J9, Thorlabs, USA). The photoacoustic optical path (MMF) with the OCT optical path (SMF) was combined into one double cladding fiber (DCF) through a custom-designed double-cladding fiber coupler (DCFC, Thorlabs, USA), which is optimized for the wavelength range from 1250 nm to 1750nm. The photoacoustic excitation beam was transmitted through both the inner cladding and core of the DCF, and the OCT beam was transmitted via the core. A custom-designed opto-electric slip ring was used to transmit both optical beam and ultrasonic signals, and drive the imaging catheter to perform 3D scanning by a rotary motor and a pull-back stage, which is similar to the design of the previous study [31]. The opto-electric slip ring was assembled co-axially with an electrical slip ring and a fiber optical rotary joint. The fiber optical rotary joint is custom-designed based on DCF, which allows the core and inner cladding of the DCF to transmit OCT and photoacoustic beam during rotation at the efficiency of 95% and 75% respectively. As shown in Fig. 1(a), the photoacoustic signal and the US signal were received by a pulser/receiver (5073PR, Olympus, Japan) with an amplifier of 39 dB.

A fully integrated miniature intravascular catheter with a diameter of 0.9 mm was custom-built as shown in Fig. 1(b), which allows tri-modality imaging. The OCT beam and photoacoustic beam were transmitted via the DCF and focused by a graded-index (GRIN) lens (Agiltron, USA), which has a cleaved angle of 8° for minimum reflectance loss and a diameter of 0.25 mm and allow operation wavelength from 600 nm to 1800nm and then reflected towards the tissue surface by a right-angle prism of 35°. A 40 MHz ultrasonic transducer (Blatek, USA, 0.5 mm (width)×0.6 mm (length)×0.2 mm (height)) was used to emit ultrasound waves and receive both photoacoustic and US signals. The optical beam and acoustic beam were overlapped between 0.6 mm and 3.6 mm from the center of the catheter, covering the normal range of the coronary artery wall. The catheter was driven by the DCF-based opto-electric slip ring to perform 360-degree rotation.

Furthermore, time synchronization in the tri-modality system was strictly controlled. The trigger signals from OPO lasers were used to synchronize tri-modality data acquisition as well as the rotation and pull-back of the slip ring. To avoid aliasing of photoacoustic and US signals, triggers for ultrasound transmission were delayed by 5 µs with a custom-made delay module. OCT signals were acquired when an OCT trigger was generated immediately after an OPO trigger. Two computers with two same data acquisition (DAQ) cards (ATS9325, Alazar Tech, Canada) were used for PA/US and OCT signal data acquisition separately. The data acquisition and display were performed in LabVIEW and all the recorded data were post-processed by MATLAB.
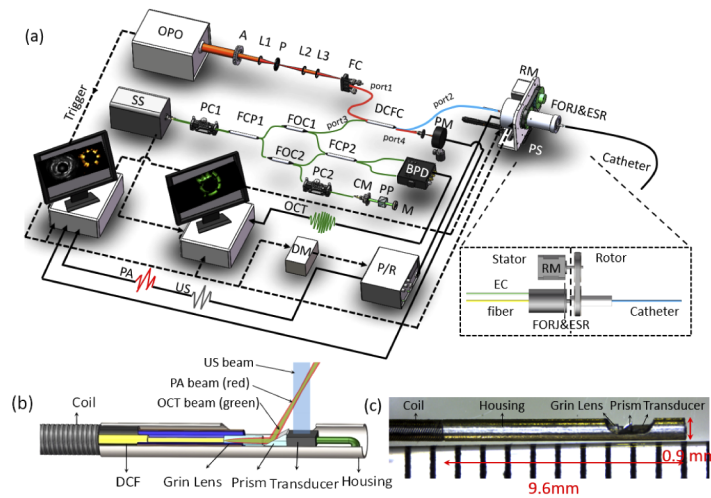
Fig. 1. (a) The MS-IVTM system overview, with an inset figure of opto-electric slip ring, (b) the tip of MS-IVTM catheter overview, and (c) photograph. OPO: optical parameter oscillator laser; A: aperture; P: pinhole; L1-L3: lens; FC: fiber connector; DCFC: double-clad fiber coupler; RM: rotary motor; PS: motorized pull-back stage; FORJ: fiber optical rotary joint; ESR: electrical slip ring; EC: electrical cable; SS: swept-source; PC1-PC2: polarization controller; PM: power meter; FCP1-FCP2: fiber optical coupler; FOC1-FOC2: fiber optical circulator; BPD: balanced amplified photodetector; CM: collimator; PP: prism pair; M: mirror; DM: delay module; P/R: ultrasound pulser/receiver; OCT: optical coherence tomography signal; US: ultrasound signal; PA: photoacoustic signal.

2.2. Imaging performance

The signal-to-noise ratio (SNR) of the tri-modality system was evaluated by imaging a black tape (for PA/US) and a mirror (for OCT) placed at different distances from the catheter. The SNR is determined by the ratio between the maximum intensity of the target and the standard deviation of the noise.

A 6-μm tungsten wire was imaged to evaluate the resolution of the system from the depth from 1 mm to 3.5 mm, except that the axial resolution of OCT was evaluated by imaging a mirror. The resolution images of tungsten wire were presented in the form of unwrapped B-scan images, with the same method stated in [32]. The resolution is determined by the full width of half maximum intensity of the tungsten wire signal. In the case of the OCT transverse resolution, the OCT profiles of the tungsten wire in lateral direction were blind-deconvoluted in order to restore the real transverse resolution of OCT based on the Richardson-Lucy algorithm [33].

2.3. Ex vivo coronary artery sample imaging with lipid identification

In the case of tri-modality imaging, one healthy porcine coronary artery with a 2.2-mm diameter stent implanted was utilized as the main part of *ex vivo* imaging sample 1. One piece of porcine subcutaneous fat and two pieces of rat-tail tendon were separately fixed with agar and inserted into the gap between the stent and the coronary artery. The sample was preserved in 4% neutered-buffered formalin and stored at 6-8 °C before imaging. During the tri-modality imaging, the artery sample was fixed inside a container filled with water at room temperature.

In the photoacoustic modality, two wavelengths (1283 nm and 1720nm) were used to distinguish lipids from collagen components. Since the absorption coefficients of water at 1720nm and 1283 nm are different, energy compensation was performed before data analysis to eliminate the attenuation of water. According to the Beer-Lambert law [34], the manually segmented

photoacoustic signal of targets was multiplied by the compensation coefficient $e^{-\mu_\lambda z}$, where μ_λ is the optical attenuation coefficient at a certain wavelength λ, z is the depth of target under water. Then the photoacoustic signals were computed through slope-based method [35]:

$$slope = \frac{I_{1720} - I_{1283}}{\lambda_{1720} - \lambda_{1283}}, \tag{1}$$

where I is the compensated intensity of the photoacoustic signal, λ is the wavelength. The slope of photoacoustic amplitude was used as a parameter to identity lipid components and can qualitatively reflect the local concentration of components [36].

In the case of spectroscopic photoacoustic imaging, another healthy porcine coronary artery was utilized as imaging sample 2, with a 3-mm stent implanted, and two porcine peripheral adipose tissues from the aorta inserted into the gap between the stent and coronary artery. The method of preservation and storage was the same as the first sample. This sample was used for spectroscopic photoacoustic imaging with 11 excitation wavelengths from 1690 nm to 1778 nm. The photoacoustic spectrum of adipose in this sample was compared with the absorption spectrum of lipid [37]. The correlation coefficient is determined by:

$$corr = \frac{\sum_{i=1}^{n}(I_i - \bar{I})(A_i - \bar{A})}{\sqrt{\sum_{i=1}^{n}(I_i - \bar{I})^2 \sum_{i=1}^{n}(A_i - \bar{A})^2}}, \tag{2}$$

where I and A are the photoacoustic signal intensity and optical absorption at different wavelengths, n is the total number of excitation wavelengths.

3. Results

3.1. Resolution and signal-to-noise ratio

According to Fig. 2(a)-(d)(h), the transverse resolution of the photoacoustic, ultrasound, and OCT image maintain 100-180 μm, 130-240 μm, and 24-44 μm respectively between the imaging range of 1 mm and 2.5 mm, which covers the range of artery wall. Correspondingly, the axial resolution of OCT is 16 μm, and ultrasound and photoacoustic can reach 35-55 μm, which is related to the bandwidth and center frequency of the ultrasound transducer. Meanwhile, the SNR performance of the system was measured with the black tape (PA/US) and mirrors (OCT). Figure 2(g) shows the SNR plots of photoacoustic, ultrasound, and OCT at different imaging depths. All three modalities have an SNR higher than 20 dB within the range of 0.6-3.2 mm. In addition, as shown in Fig. 2(g), photoacoustic have better resolution and SNR within the image range of 1-2 mm, due to the smaller focused optical beam size in this overlap area.

3.2. Ex vivo sample tri-modality images

As shown in Fig. 3, tri-modality images of the *ex vivo* sample 1, were obtained simultaneously, with a rotation speed of 0.75 rad/min and a pull-backing step of 100 μm. Figure 3(a)-(c) shows the photoacoustic, OCT, and US B-scan images of sample 1 at the same site respectively. Figure 3(a) shows porcine subcutaneous fat had a higher photoacoustic signal than tail tendon since lipid has a higher optical absorption coefficient than collagen at an excitation wavelength of 1720nm. Figure 3(b) and Fig. 3(c) show the high-resolution images of stent structure and strut coverage inside the vessel by OCT, and the whole blood vessel wall image of IVUS. Figure 3(d) shows the merged tri-modality image. The total computational time of each PA/US and OCT B-scan image is 2.6 s and 2.5 s respectively. The 3D volume images of photoacoustic, OCT, and US were shown in Fig. 3(e)-(g). OCT and US images show the morphological information of fat and tendon tissues, while photoacoustic images indicated the chemical composition of tissues based on their optical absorption characteristics. However, there are still difficulties to identify the lipid
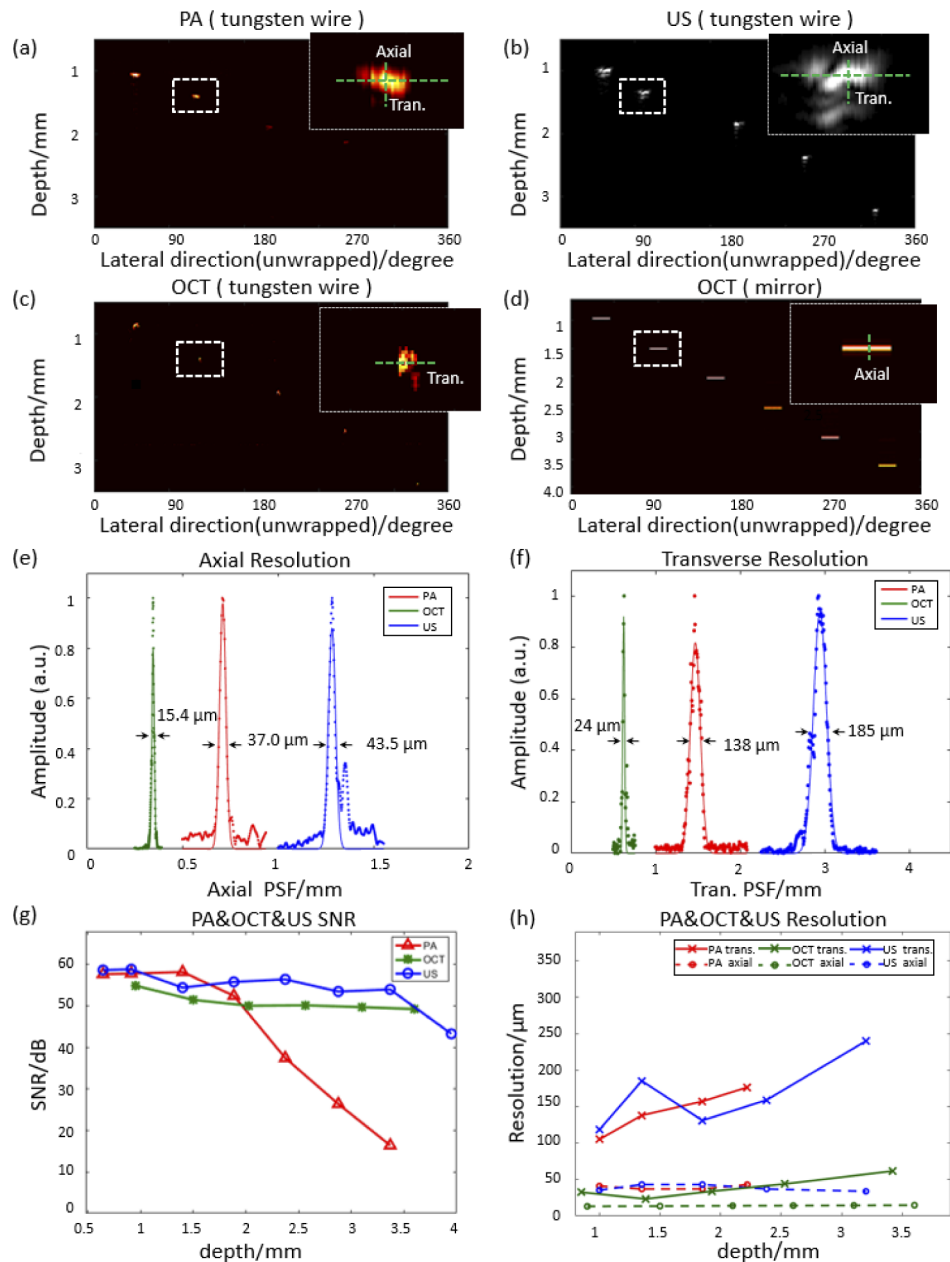
Fig. 2. PA/US/OCT resolution and SNR of the MS-IVTM system. (a)-(c) unwrapped PA/US/OCT B-scan images of the tungsten wire (~6 μm) at different imaging depths. (d) unwrapped OCT B-scan image of the mirror at different depths. And the insets in (a)-(d) show an enlarged view of the targets around 1.5 mm. (e), (f) Axial and transverse resolution of three imaging modalities from the enlarged view of the dashed box in (a)-(d) respectively. (g) Signal-to-noise ratio (SNR) of PA/US/OCT at different depths. (h) Resolution of PA/US/OCT at different depths with different targets.

component from another component at a single wavelength, especially when the concentration of components is unknown.
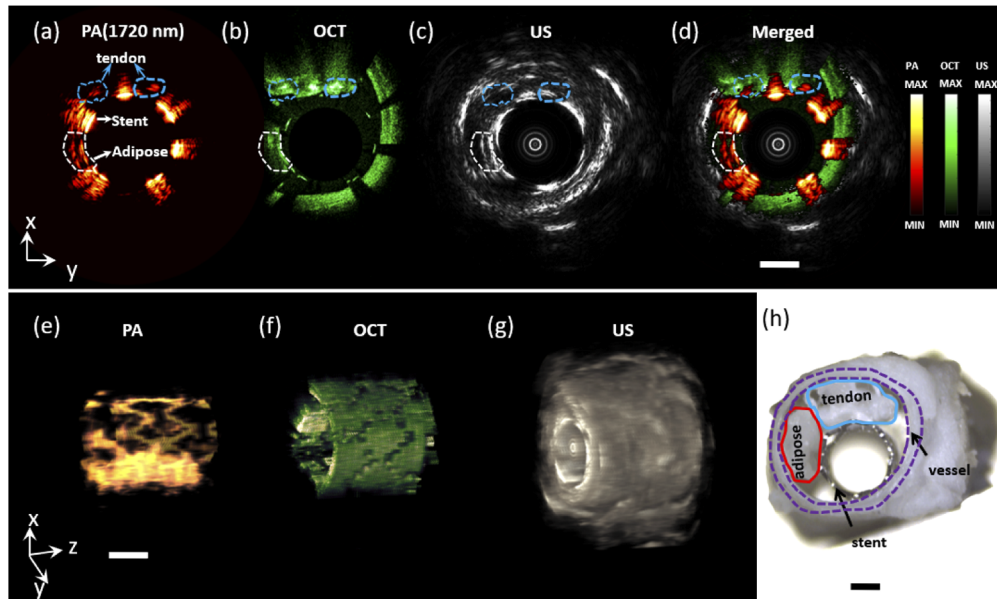

Fig. 3. Cross-sectional and three-dimensional (3D) tri-modality images of the phantom. (a)-(c) PA (1720nm), OCT, and US B-scan image respectively. (d) Merged tri-modality image. (e)-(g) PA, OCT, and US 3D image. (h) Phantom photograph. Scale bar: 1 mm

In order to interrogate the composition, dual wavelengths (1283 nm and 1720 nm) were chosen to perform photoacoustic imaging in Fig. 4(a)(b), since they are the absorption peak for collagen and lipid respectively. The enlarged view of target regions 1, 2, and 3, marked by white dashed circles, were laid on left and right side of Fig. 4(a)(b). The gradient ratio of region 1 was mostly positive, while that of region 2 and 3 was mostly negative. It suggested that the absorption coefficient of the substance in region 1 was greater at 1720 nm than at 1283 nm, and it was oppositive in region 2 and 3, which proved that the composition in region 1 is different from that in region 2 and 3. Then, the gradient ratios at each pixel in three regions from dual-wavelength images were overlaid to the photoacoustic B-scan image, as shown in Fig. 4(c). With dual-wavelength excitation, the gradient ratio method can distinguish one component from another through their respective absorption peak.

3.3. Spectroscopic photoacoustic imaging

Dual-wavelength excitation of photoacoustic imaging can do help to distinguish lipids from another component, but it is necessary to compare the photoacoustic signal at multiple wavelengths with the absorption spectrum of lipids in order to identify lipids from multiple components or evaluate their concentration. Another porcine coronary artery sample with porcine peripheral adipose inside was utilized for spectroscopic photoacoustic imaging at 11 wavelengths from 1690 nm to 1778nm with a pulse energy of 15 μJ, as shown in Fig. 5(a)-(h). The amplitude of the photoacoustic signal within the white dashed area is significantly higher at 1720nm than that at other wavelengths. Then, the spectroscopic photoacoustic signal plot was compared with the optical absorption spectrum of lipid [37], as shown in Fig. 5(i). The correlation coefficient between the experimental photoacoustic spectrum and the absorption spectrum was calculated for each pixel, indicating abundant lipid deposition within the region 1 and 2. Figure 5(j) shows
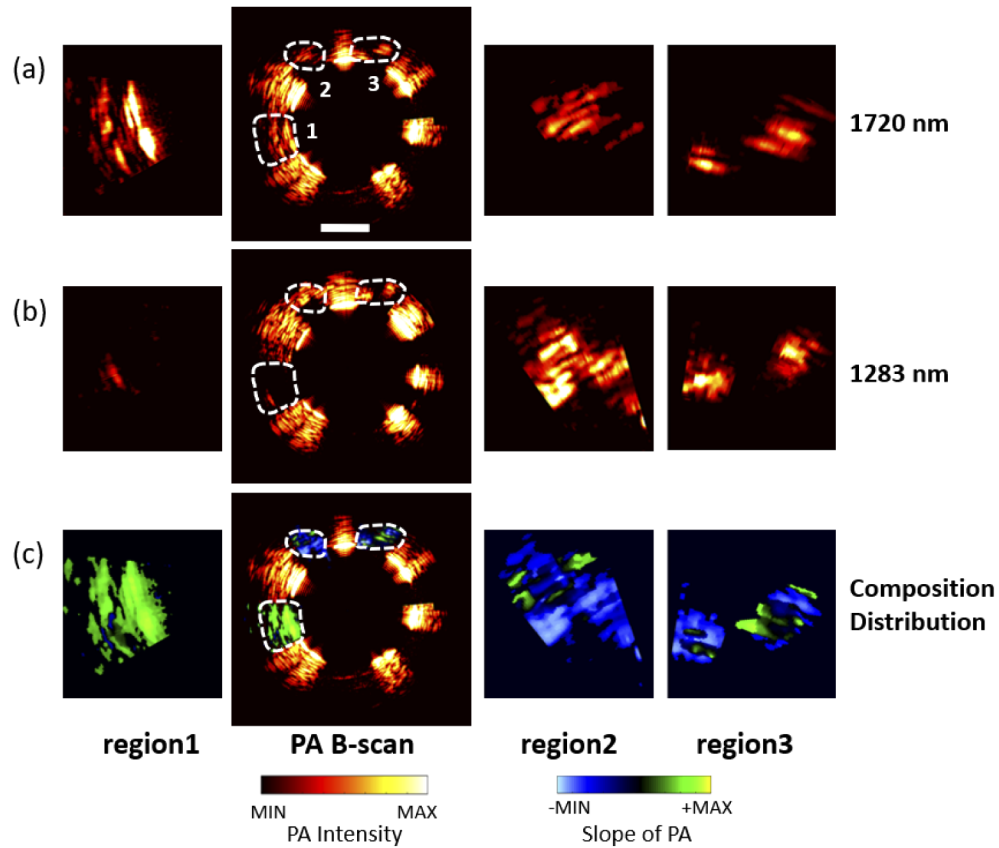
Fig. 4. Adipose and tendon photoacoustic images at two wavelengths (1720nm and 1283 nm) and distribution analysis results. (a),(b) photoacoustic B-scan image at 1720nm and 1283 nm. Left: the enlarged image of the region 1; Center: B-scan image; Right: enlarged images of the region 2 and region 3. (c) The slope results of region1, 2, and 3. Left: enlarged view of the slope of region 1; Right: enlarged view of the slope of region 2,3; Center: the slope of region1, 2,3 remapping to the photoacoustic B-scan image. Scale bar: 1 mm

the mapping of the correlation coefficient, which suggests the spatial distribution of the adipose concentration.
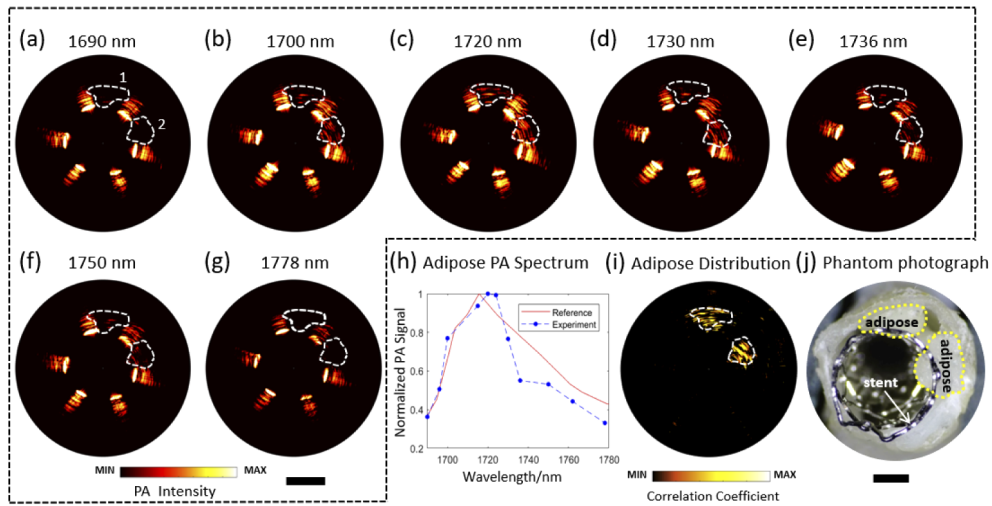
Fig. 5. Spectroscopic PA images of the peri-adventitial adipose tissue from a porcine aorta segment. (a)-(g) Representative PA B-scan images from 1690 nm to 1778nm. (h) Experimental PA spectroscopic result and optical absorption spectrum [37] of peri-adventitial adipose tissue. (i) Distribution of adipose concentration mapping by correlation calculation. (j) Phantom photograph. Scale bar: 1 mm

4.   Discussion

Both morphological and functional information of plaque is important for research and diagnosis of the vulnerable plaque. Multi-modality intravascular imaging has been developed for obtaining comprehensive information, but some problems still hinder the application of this new technology, such as over-large catheters, non-rotational scanning, and lack of quantitative analysis of lipid components. In this study, for the first time, an MS-IVTM system with a miniature imaging catheter was developed, which allowed continuous 360-degree rotational PA/US/OCT imaging, including spectroscopic photoacoustic imaging.

Compared to the previous tri-modality catheter of coaxial design [30], we performed a non-coaxial setup in order to reduce the size of the catheter. The configuration of the transducer allows the outer diameter of our catheter remains only 0.9 mm, which is, to our knowledge, the smallest tri-modality catheter currently. Furthermore, the non-coaxial design avoids additional acoustic attenuation through acoustic reflection prisms in the coaxial design, which decreases the transition efficiency of the acoustic signal [38]. Meanwhile, the imaging performance indicated a relatively high SNR within the imaging range from 0.6 to 3.2 mm, which fits the size of the lumen and depth of the wall to satisfy the needs of intravascular imaging. Although the SNR reduces rapidly over 3.2 mm, it does not affect the application of imaging atherosclerotic plaques. Additionally, the GRIN lens in our catheter was fused at the tip of DCF, in order to transmit both OCT and photoacoustic beams and reduce the reflectance at the surfaces between DCF and GRIN lens. Due to the difficulties of fusion splicing a small diameter fiber to a large diameter GRIN lens, the diameter of the GRIN lens is limited to 0.25 mm, which leads to poor focal performance within the desired working range. Therefore, both transverse resolutions of OCT and photoacoustic are compromised. In future works, a 0.5-mm GRIN lens can be used to lead to a better resolution for OCT and photoacoustic modalities, if the fusion problem can be solved.

The *ex vivo* samples were made from stents, porcine subcutaneous fat, peripheral adipose, rat-tail tendon, and porcine coronary arteries, to mimic stent-implanted coronary arteries with lipid-rich or collagen-rich plaque, referring to previous studies [39–41]. Through the experiments

of these *ex vivo* samples, it was indicated that OCT can evaluate the stent structure and have access to stent strut coverage with the vessel wall clearly, IVUS can offer the entire vascular structural information, and photoacoustic can offer the depth-involved lipid-deposition information with high contrast. Through the difference of photoacoustic signals, the dual-wavelength (1283 nm and 1720nm) results demonstrated the ability of the MS-IVTM system to detect and distinguish lipids from collagen components effectively. Moreover, multi-spectral photoacoustic excitation was applied to the *ex vivo* vessel sample with porcine peripheral adipose tissues inside, which have been used to mimic plaque lesions [40]. The photoacoustic spectrum results from the adipose tissues show a high correlation with the optical absorption spectrum of lipid. But the correlation coefficients, which represent the lipid concentration, vary from the different regions of the adipose tissues. Therefore, with multi-spectral excitation, the spectroscopic photoacoustic images can result in the spatial distribution of the lipid concentration from the correlation computing map.

In the scenario of IVPA imaging of lipids, it is important to maintain a high SNR of targets. The upper limit of SNR mainly depends on the optical fluence illuminated on the targets. Because of the relatively weak optical absorption of lipids, the precise determination of the photoacoustic spectrum and concentration quantification is sensitive to signal intensity. Therefore, MMF-based catheters are commonly used to deliver large energy [17,18], although SMF can result in a better resolution of photoacoustic imaging. In the case of the tri-modality system, however, the OCT modality can only work in single mode to precisely control its optical path length. There is a dilemma between OCT and spectroscopic photoacoustic imaging through a single channel. In this work, we designed and manufactured a DCF-based catheter to resolve the problem of using MMF or SMF. The OCT and photoacoustic optical path can utilize the core and first cladding of DCF respectively. Utilization of core guarantees the stable coherence condition of OCT, and first cladding with a bigger diameter can help transmit enough optical energy to the surface of the tissue in order for spectroscopic photoacoustic imaging. The maximum optical fluence of excitation (80 mJ/cm^2) is lower than the ANSI safety limit of 1 J/cm^2 between 1500 nm and 1800nm [42]. Higher energy under ANSI safety criteria can be delivered to the targets to improve SNR by increasing the optical coupling efficiency of our system. Furthermore, the IVPA modality, with a resolution of 100-300 μm, in the MS-IVTM system is sufficient for imaging lipids in the necrotic core, which reach the size of the submillimeter scale [43]. The upper limit of the photoacoustic transverse resolution is related to the numerical aperture (NA) of the optical system, which depends on the core diameter and NA of fiber and the focal ability of the GRIN lens. As a result, our DCF-based catheter design can achieve deeper penetration with sufficient resolution and SNR to image and distinguish rich lipids in plaques in IVPA modality and maintain a high resolution of IVOCT imaging simultaneously.

In addition, our MS-IVTM system achieved three-dimensional imaging with continuous rotational scanning with pull-backing. Unlike imaging by an array detector, mechanical scanning is essential for point-by-point imaging by a single element detector. For intravascular imaging, rotational scanning combined with pull-backing is a reasonable method, which has been proved in the clinical application [17,24,25,44]. Thus, an optical rotary or slip ring is important, which can connect the stator with the rotor to transmit continuous signals from the source to the tip of the catheter and backward during the rotational scanning. In addition, the utility of rotary joint allows 360-degree rotation and full field-of-view of samples, compared to previous micromotor-based mirror-rotating scanning methods, which lost partial view due to the blocking of the electric wires [45]. However, multi-optical modality usually requires the optical rotary to connect several fibers, which increases the difficulty of design and assembly of optical rotary and the catheter connected to maintain suitable transmission stability and efficiency. The customized optical rotary joint based on DCF reduced the engineering challenge dramatically.

There are still a few improvements to our MS-IVTM system to be obtained in the future. Firstly, in the case of intravascular imaging *in vivo*, flushing is commonly used to reduce the

effect of optical scattering of blood, especially in IVOCT. However, water has a strong optical absorption around the wavelength of 1700nm, which has an effect on lipid detection. Therefore, flushing fluid with low optical absorption is required for intravascular tri-modality imaging in the future. Secondly, the image speed is limited by the low repetition OPO laser source (10 Hz). Therefore, *in vivo* images will be affected by the movement of breathing and other artifacts. High repetition and high energy laser source around 1700nm wavelength is appreciated, for spectroscopic photoacoustic imaging of lipid component. Thirdly, the lipid components used in this paper are peri-adventitial adipose instead of cholesterol deposition in the necrotic core. Future studies will focus on imaging atherosclerosis models or vessels *in vivo*. Fourthly, the correlation coefficient between photoacoustic spectroscopic results and the absorption spectrum of a certain component in a complex environment can suggest its concentration quantitatively but not qualitatively. Previous methods of concentration analysis require both multi-wavelength photoacoustic detection and the spectrum information of major components in the complex environment, which consume a long detection time. Thus, a new analytic method for concentration calculation shall be optimized to balance the imaging speed and selection of photoacoustic wavelengths. Finally, clinical intravascular applications require the outer diameter of imaging catheters < 1 mm and rigid length < 5 mm, in order to access the small branches of coronary arteries [46]. The diameter of our catheter is 0.9 mm, which satisfies the needs. However, the 9.6-mm rigid part of our catheter is oversize for clinical applications. The reason is that the fiber coating at the DCF tip, with a total length of about 5 mm, was stripped to fusion splice the DCF to the GRIN lens. Therefore, this part of the catheter required special protection with UV glue, which occupies the majority of the rigid part of our catheter. Future work will consider how to recoat the stripped fiber, restore its flexibility, and reduce the rigid length of the catheter.

5. Conclusion

In summary, we present a novel intravascular tri-modality imaging system, including US, OCT, and photoacoustic imaging with multi-spectroscopic imaging ability. To our knowledge, this is the first PA/US/OCT tri-modality imaging system that can achieve continuous 360-degree rotation and pull-backing within vessels, through a fine catheter with a diameter of mere 0.9 mm. The imaging results of the macroscopic morphology and microstructure of the blood vessels were obtained by IVUS/IVOCT, and the identification of lipid composition and the analysis of lipid concentration distribution were performed by photoacoustic spectroscopy. Our MS-IVTM system has the potential to evaluate rich lipid deposition in the necrotic core, fibrous cap covered, and stenosis comprehensively; in the future, it has the potential to be translated into the clinic to provide an effective tool for a comprehensive evaluation of atherosclerotic plaques.

Disclosures. The authors declare that there are no conflicts of interest related to this article.

Data availability. Data underlying the results presented in this paper are not publicly available at this time but may be obtained from the authors upon reasonable request.

References

1. J. Sanz and Z. A. Fayad, "Imaging of atherosclerotic cardiovascular disease," Nature **451**(7181), 953–957 (2008).
2. R. S. Rosenson, H. B. Brewer Jr, B. J. Ansell, P. Barter, M. J. Chapman, J. W. Heinecke, A. Kontush, A. R. Tall, and N. R. Webb, "Dysfunctional HDL and atherosclerotic cardiovascular disease," Nat. Rev. Cardiol. **13**(1), 48–60 (2016).
3. R. S. Rosenson, H. B. Brewer, P. J. Barter, J. L. M. Björkegren, M. J. Chapman, D. Gaudet, D. S. Kim, E. Niesor, K. A. Rye, M. F. Sacks, J. C. Tardif, and R.A. Hegele, "HDL and atherosclerotic cardiovascular disease: Genetic insights into complex biology," Nat. Rev. Cardiol. **15**(1), 9–19 (2018).

4. M. Naghavi, P. Libby, E. Falk, S. W. Casscells, S. Litovsky, J. Rumberger, J. J. Badimon, C. Stefanadis, P. Moreno, G. Pasterkamp, Z. Fayad, P. H. Stone, S. Waxman, P. Raggi, M. Madjid, A. Zarrabi, A. Burke, C. Yuan, P. J. Fitzgerald, D. S. Siscovick, C. L. de Korte, M. Aikawa, K. E. J. Airaksinen, G. Assmann, C. R. Becker, J. H. Chesebro, A. Farb, Z. S. Galis, C. Jackson, I.-K. Jang, W. Koenig, R. A. Lodder, K. March, J. Demirovic, M. Navab, S. G. Priori, M. D. Rekhter, R. Bahr, S. M. Grundy, R. Mehran, A. Colombo, E. Boerwinkle, C. Ballantyne, W. Insull Jr, R. S. Schwartz, R. Vogel, P. W. Serruys, G. K. Hansson, D. P. Faxon, S. Kaul, H. Drexler, P. Greenland, J. E. Muller, R. Virmani, P. M. Ridker, D. P. Zipes, P. K. Shah, and J. T. Willerson, "From vulnerable plaque to vulnerable patient: A call for new definitions and risk assessment strategies: Part I," Circulation **108**(14), 1664–1672 (2003).
5. R. Virmani, A. P. Burke, A. Farb, and F. D. Kolodgie, "Pathology of the vulnerable plaque," J. Am. Coll. Cardiol. **47**(8), C13–C18 (2006).
6. E. Falk, P. K. Shah, and V. Fuster, "Coronary plaque disruption," Circulation **92**(3), 657–671 (1995).
7. G. W. Stone, A. Maehara, Z. A. Ali, C. Held, M. Matsumura, L. Kjøller-Hansen, H. E. Bøtker, M. Maeng, T. Engstrøm, R. Wiseth, J. Persson, T. Trovik, U. Jensen, S. K. James, G. S. Mintz, O. Dressler, A. Crowley, O. Ben-Yehuda, and D. Erlinge, "Percutaneous coronary intervention for vulnerable coronary atherosclerotic plaque," J. Am. Coll. Cardiol. **76**(20), 2289–2301 (2020).
8. R. D. Madder, R. Puri, J. E. Muller, J. Harnek, M. Götberg, S. VanOosterhout, M. Chi, D. Wohns, R. McNamara, K. Wolski, S. Madden, S. Sidharta, J. Andrews, S. J. Nicholls, and D. Erlinge, "Confirmation of the intracoronary near-infrared spectroscopy threshold of lipid-rich plaques that underlie ST-segment-elevation myocardial infarction," Arterioscler., Thromb., Vasc. Biol. **36**(5), 1010–1015 (2016).
9. S. Karlsson, E. Anesäter, K. Fransson, P. Andell, J. Persson, and D. Erlinge, "Intracoronary near-infrared spectroscopy and the risk of future cardiovascular events," Open Heart **6**(1), e000917 (2019).
10. H. M. Garcia-Garcia, M. A. Costa, and P. W. Serruys, "Imaging of coronary atherosclerosis: intravascular ultrasound," Eur. Heart J. **31**(20), 2456–2469 (2010).
11. B. E. Bouma, M. Villiger, K. Otsuka, and W.-Y. Oh, "Intravascular optical coherence tomography [Invited]," Biomed. Opt. Express **8**(5), 2660 (2017).
12. M. W. Lee, J. W. Song, W. J. Kang, H. S. Nam, T. S. Kim, S. Kim, W.-Y. Oh, J. W. Kim, and H. Yoo, "Comprehensive intravascular imaging of atherosclerotic plaque in vivo using optical coherence tomography and fluorescence lifetime imaging," Sci. Rep. **8**(1), 14561 (2018).
13. J. W. Verjans, E. A. Osborn, G. J. Ughi, M. A. Calfon, E. Hamidi, A. P. Antoniadis, M. I. Papafaklis, M. F. Conrad, P. Libby, P. H. Stone, R. P. Cambria, G. J. Tearney, and F. A. Jaffer, "Targeted Near-Infrared Fluorescence Imaging of Atherosclerosis: Clinical and Intracoronary Evaluation of Indocyanine Green," JACC Cardiovasc. Imaging **9**(9), 1087–1095 (2016).
14. M.-J. Bertrand, M. Abran, F. Maafi, D. Busseuil, N. Merlet, T. M. Avram, P. Geoffroy, P.-L. Tardif, A. Abulrob, M. A. Ghahroudi, F. Ni, M. Sirois, P. L. L'Allier, É. Rhéaume, F. Lesage, and J.-C. Tardif, "In vivo near-infrared fluorescence imaging of atherosclerosis using local delivery of novel targeted molecular probes," Sci. Rep. **9**(1), 1–12 (2019).
15. R. Waksman, C. D. Mario, R. Torguson, Z. A. Ali, V. Singh, W. H. Skinner, A. K. Artis, T. T. Cate, E. Powers, C. Kim, E. Regar, S. C. Wong, S. Lewis, J. Wykrzykowska, S. Dube, S. Kazziha, M. van der Ent, P. Shah, P. E. Craig, Q. Zou, P. Kolm, H. B. Brewer, H. M. G. Garcia, H. Samady, J. Tobis, M. Zainea, W. Leimbach, D. Lee, T. Lalonde, W. Skinner, A. Villa, H. Liberman, G. Younis, R. de Silva, M. Diaz, L. Tami, J. Hodgson, G. Raveendran, N. Goswami, J. Arias, L. Lovitz, R. Carida II, S. Potluri, F. Prati, A. Erglis, A. Pop, M. McEntegart, M. Hudec, U. Rangasetty, and D. Newby, "Identification of patients and plaques vulnerable to future coronary events with near-infrared spectroscopy intravascular ultrasound imaging: a prospective, cohort study," Lancet **394**(10209), 1629–1637 (2019).
16. H. P. Buschman, E. T. Marple, M. L. Wach, B. Bennett, T. C. B. Schut, H. A. Bruining, A. V. Bruschke, A. van der Laarse, and G. J. Puppels, "In vivo determination of the molecular composition of artery wall by intravascular Raman spectroscopy," Anal. Chem. **72**(16), 3771–3775 (2000).
17. K. Jansen, A. F. W. van der Steen, H. M. M. van Beusekom, J. W. Oosterhuis, and G. van Soest, "Intravascular photoacoustic imaging of human coronary atherosclerosis," Opt. Lett. **36**(5), 597 (2011).
18. Y. Cao, J. Hui, A. Kole, P. Wang, Q. Yu, W. Chen, M. Sturek, and J.-X. Cheng, "High-sensitivity intravascular photoacoustic imaging of lipid-laden plaque with a collinear catheter design," Sci. Rep. **6**(1), 1–8 (2016).
19. T. Buma, N. C. Conley, and S. W. Choi, "Multispectral photoacoustic microscopy of lipids using a pulsed supercontinuum laser," Nat. Biotechnol. **18**(4), 87–101 (2017).
20. Y. Cao, A. Kolea, L. Lan, P. Wang, J. Hui, M. Sturek, and J.-X. Cheng, "Spectral analysis assisted photoacoustic imaging for lipid composition differentiation," Photoacoustics **7**, 12–19 (2017).
21. J. A. Schaar, A. F. W. van der Steen, F. Mastik, R. A. Baldewsing, and P. W. Serruys, "Intravascular palpography for vulnerable plaque assessment," J. Am. Coll. Cardiol. **47**(8), C86–C91 (2006).
22. J. Tian, H. Dauerman, C. Toma, H. Samady, T. Itoh, S. Kuramitsu, T. Domei, H. Jia, R. Vergallo, T. Soeda, S. Hu, Y. Minami, H. Lee, B. Yu, and I. Jang, "Prevalence and characteristics of TCFA and degree of coronary artery stenosis: An OCT, IVUS, and angiographic study," J. Am. Coll. Cardiol. **64**(7), 672–680 (2014).
23. S. Lee, M. W. Lee, H. S. Cho, J. W. Song, H. S. Nam, D. J. Oh, K. Park, W. Oh, H. Yoo, and J. W. Kim, "Fully integrated high-speed intravascular optical coherence tomography/near-infrared fluorescence structural/molecular imaging in vivo using a clinically available near-infrared fluorescence-emitting indocyanine green to detect inflamed lipid-rich atheromata in coronary-sized vessels," Circ. Cardiovasc. Interv. **7**(4), 560–569 (2014).

24. J. Li, T. Ma, D. Mohar, E. Steward, M. Yu, Z. Piao, Y. He, K. K. Shung, Q. Zhou, P. M. Patel, and Z. Chen, "Ultrafast optical-ultrasonic system and miniaturized catheter for imaging and characterizing atherosclerotic plaques in vivo," Sci. Rep. **5**(1), 18406 (2015).

25. S. J. Mathews, C. Little, C. D. Loder, R. D. Rakhit, W. Xia, E. Z. Zhang, P. C. Beard, M. C. Finlay, and A. E. Desjardins, "All-optical dual photoacoustic and optical coherence tomography intravascular probe," Photoacoustics **11**, 65–70 (2018).

26. J. Hui, Y. Cao, Y. Zhang, A. Kole, P. Wang, G. Yu, G. Eakins, M. Sturek, W. Chen, and J.-X. Cheng, "Real-Time intravascular photoacoustic-ultrasound imaging of lipid-laden plaque in human coronary artery at 16 frames per second," Sci. Rep. **7**(1), 1–11 (2017).

27. Y. Yang, X. Li, T. Wang, P. D. Kumavor, A. Aguirre, K. K. Shung, Q. Zhou, M. Sanders, M. Brewer, and Q. Zhu, "Integrated optical coherence tomography, ultrasound and photoacoustic imaging for ovarian tissue characterization," Biomed. Opt. Express **2**(9), 2551 (2011).

28. P. Montorsi, P. M. Ravagnani, S. Galli, F. Rotatori, A. Briganti, A. Salonia, P. Rigatti, and F. Montorsi, "The artery size hypothesis: a macrovascular link between erectile dysfunction and coronary artery disease," Am. J. Cardiol. **96**(12), 19–23 (2005).

29. X. Dai, L. Xi, C. Duan, H. Yang, H. Xie, and H. Jiang, "Miniature probe integrating optical-resolution photoacoustic microscopy, optical coherence tomography, and ultrasound imaging: proof-of-concept," Opt. Lett. **40**(12), 2921 (2015).

30. X. Dai, H. Yang, T. Shan, H. K. Xie, S. A. Berceli, and H. Jiang, "Miniature endoscope for multimodal imaging," ACS Photonics **4**(1), 174–180 (2017).

31. S. Liang, T. Ma, J. Jing, X. Li, J. Li, K. K. Shung, Q. Zhou, J. Zhang, and Z. Chen, "Trimodality imaging system and intravascular endoscopic probe: combined optical coherence tomography, fluorescence imaging and ultrasound imaging," Opt. Lett. **39**(23), 6652 (2014).

32. Y. Li, R. Lin, C. Liu, J. Chen, H. Liu, R. Zheng, X. Gong, and L. Song, "In vivo photoacoustic/ultrasonic dual-modality endoscopy with a miniaturized full field-of-view catheter," J. Biophotonics **11**(10), e201800034 (2018).

33. D. A. Fish, A. M. Brinicombe, E. R. Pike, and J. G. Walker, "Blind deconvolution by means of the Richardson-Lucy algorithm," J. Opt. Soc. Am. A **12**(1), 58 (1995).

34. E. Park, Y.-J. Lee, C. Lee, and T. J. Eom, "Effective photoacoustic absorption spectrum for collagen-based tissue imaging," J. Biomed. Opt. **25**(05), 1 (2020).

35. B. Wang, J. L. Su, J. Amirian, S. H. Litovsky, R. Smalling, and S. Emelianov, "Detection of lipid in atherosclerotic vessels using ultrasound-guided spectroscopic intravascular photoacoustic imaging," Opt. Express **18**(5), 4889 (2010).

36. B. Wang, P. Joshi, V. Sapozhnikova, J. Amirian, S. H. Litovsky, R. Smalling, K. Sokolov, and S. Emelianov, "Intravascular photoacoustic imaging of macrophages using molecularly targeted gold nanoparticles," Proc. SPIE **7564**, 75640A (2010).

37. R. R. Anderson, W. Farinelli, H. Laubach, D. Manstein, A. N. Yaroslavsky, J. Gubeli III, K. Jordan, G. R. Neil, M. Shinn, W. Chandler, G. P. Williams, S. V. Benson, D. R. Douglas, and H. F. Dylla, "Selective photothermolysis of lipid-rich tissues: A free electron laser study," Lasers Surg. Med. **38**(10), 913–919 (2006).

38. S. Hu, K. Maslov, and L. V. Wang, "Second-generation optical-resolution photoacoustic microscopy with improved sensitivity and speed," Opt. Lett. **36**(7), 1134 (2011).

39. T. L. P. Slottow, R. Pakala, T. Okabe, D. Hellinga, R. J. Lovec, F. O. Tio, A. B. Bui, and R. Waksman, "Optical coherence tomography and intravascular ultrasound imaging of bioabsorbable magnesium stent degradation in porcine coronary arteries," Cardiovasc. Revascularization Med. **9**(4), 248–254 (2008).

40. M. Wu, G. Springeling, M. Lovrak, F. Mastik, S. Iskander-Rizk, T. Wang, H. M. M. van Beusekom, A. F. W. van der Steen, and G. Van Soest, "Real-time volumetric lipid imaging in vivo by intravascular photoacoustics at 20 frames per second," Biomed. Opt. Express **8**(2), 943 (2017).

41. P. Wang, P. Wang, H.-W. Wang, and J.-X. Cheng, "Mapping lipid and collagen by multispectral photoacoustic imaging of chemical bond vibration," J. Biomed. Opt. **17**(9), 0960101 (2012).

42. Laser Institute of America, American National Standard for Safe Use of Lasers ANSI Z136.1 - 2014 (American National Standards Institute, Inc., 2014).

43. W. Insull Jr, "The pathology of atherosclerosis: plaque development and plaque responses to medical treatment," Am. J. Med. **122**(1), S3–S14 (2009).

44. G. Guagliumi and V. Sirbu, "Optical coherence tomography: High resolution intravascular imaging to evaluate vascular healing after coronary stenting," Catheter. Cardiovasc. Interv. **72**(2), 237–247 (2008).

45. J.-M. Yang, C. Li, R. Chen, B. Rao, J. Yao, C.-H. Yeh, A. Danielli, K. Maslov, Q. Zhou, K. K. Shung, and L. V. Wang, "Optical-resolution photoacoustic endomicroscopy in vivo," Biomed. Opt. Express **6**(3), 918–932 (2015).

46. Y. Li, J. Chen, and Z. Chen, "Multimodal intravascular imaging technology for characterization of atherosclerosis," J. Innov. Opt. Health Sci. **13**(01), 2030001 (2020).